HYDROGEN TRAPPING BY IRRADIATION-INDUCED DEFECTS IN 316L STAINLESS STEEL

Anne-Cécile BACH[1,2]**, Frantz MARTIN**[1]**, Cécilie DUHAMEL**[2]**, Stéphane PERRIN**[3]**, François JOMARD**[4]**, Jérôme CREPIN**[2]

[1]*DEN-Service de la Corrosion et du Comportement des Matériaux dans leur Environnement (SCCME), CEA, Université Paris-Saclay, F-91191, Gif-sur-Yvette, France*
[2]*MINES ParisTech, PSL Research University, MAT- Centre des matériaux, CNRS UMR 7633, BP 87, 91003 Evry, France*
[3]*CEA, DEN, DE2D, SEAD, Laboratoire d'étude des Ciments et Bitumes pour le Conditionnement, F-30207 Bagnols-sur-Cèze, France*
[4]*Groupe d'Etude de la Matière Condensée, CNRS, UVSQ, 45 avenue des Etats-Unis, 78035 Versailles cedex, France*

Abstract

The irradiation-induced defects in stainless steel internal components of pressurized water reactors combined with hydrogen uptake during the oxidation process could be a key parameter in the mechanism for Irradiation-Assisted Stress Corrosion Cracking (IASCC). The ultimate aim of this study is to characterize the effects of irradiation defects on hydrogen uptake during the oxidation of an austenitic stainless steel (SS) in primary water. The focus was made on the interactions between hydrogen and these defects. A heat-treated 316L SS containing a low amount of defects is compared with ion implanted samples. Both materials were characterized by Transmission Electron Microscopy (TEM). Hydrogen uptake was then promoted by cathodic charging using deuterium as isotopic tracer for hydrogen. The deuterium distribution was first characterized by SIMS (Secondary Ion Mass Spectrometry) profiles. This technique highlighted some deuterium segregation in link with the localization of implantation-induced defects, i.e. dislocation loops and cavities. Using TDS (Thermal Desorption Spectrometry) experimental results and literature data, a numerical model was used to simulate the deuterium profiles, providing diffusion and trapping/detrapping information associated with irradiation defects in the 316L SS.

Keywords

Hydrogen trapping, Irradiation defects, Austenitic stainless steel, Thermal desorption, Modeling

Introduction

Austenitic stainless steels are currently used for several structural components of Light Water Reactors (LWR) as the vessel internals and the associated baffles and bolts in the reactor core. In Pressurized Water Reactor (PWR) the austenitic stainless steels (SS) are exposed to primary water, which is an aqueous solution containing dissolved hydrogen at a temperature ranging between 290 °C and 325 °C and a pressure of about 155 bar. These materials are subjected to a corrosive environment, mechanical and thermal stresses and also to the neutron flux emitted by the nuclear fuel in the reactor core. Since the eighties, some cracks have been observed on SS baffles and bolts in the reactor core. They could result from a phenomenon of Irradiation-Assisted Stress Corrosion Cracking (IASCC) although all the mechanisms are not totally understood yet [1], [2].

A recent study of Dumerval *et al*. [3] highlighted, thanks to the GD-OES (Glow discharge Optical Emission Spectroscopy) technique, that a non-negligible amount of hydrogen was incorporated and trapped underneath the oxide/alloy interface during oxidation of 316L SS in simulated PWR primary conditions. Indeed, the primary water is a potential huge source of hydrogen (water and dissolved hydrogen) which can dissociate, for instance in the oxidation process, then diffuse in the alloy and interact with structural defects where it could be trapped. As an illustration, in Dumerval's work [3], the accumulation of hydrogen near the oxide/alloy interface was assigned to trapping at vacancies that were created by cationic growth of the oxide layer. Hydrogen is known to alter mechanical properties of materials at room temperature [4]–[6] and may have an impact at high temperature, during surface condition transients such as crack propagation, or at least during temperature transients occurring in the reactor (e.g. for maintenance or fuel replacement).

During in-core nuclear power plant exposure conditions, interactions of neutrons with the alloy atoms induce the creation of structural defects such as vacancies, interstitials, cavities, He bubbles, black dots, dislocation loops… [7]–[11]. All these defects could be additional trapping sites for hydrogen. The main difficulty in studying hydrogen uptake during PWR exposure stands in the activation of materials under neutron flux that renders analysis much more complex than a 'simple' autoclave exposure. For this reason, a way to cover the whole effects that could affect the integrity of the vessel internals is to study these effects separately then combined in a segmented way, allowing the behavior comparison between pre-irradiated materials and a reference material.

To emulate neutron irradiation defects while avoiding difficulties of neutron irradiation experiments (time, cost, activation…), ion implantation of light or heavy ions are often used. Light ion implantation, like protons, lead to the formation of dislocation loops with a density and a mean size in the same order of magnitude that those created by neutrons irradiation as explained by Was [12], [13]. Moreover some other irradiation characteristics are also in good agreement with neutron-irradiation results like grain boundary microchemistry or radiation hardening. However, it is difficult to reach relevant damage and damage rate with protons implantations so heavy ions implantations are sometimes used. They allow the creation of a lot of damages in short times but their penetration depth is smaller (1-2 µm) than for neutron irradiation. The implanted microstructure presents the same type of defects (dislocations loops and cavities) as neutron-irradiated material.

For this study, although there exist some differences with neutron induced defects, iron ion implantations was chosen to create defects with quite similar nature and relevant in terms of

density and size to start to investigate the interactions between hydrogen and irradiation defects. Iron ions were also chosen to minimize the modifications induced by implantation on the average alloy composition (main alloying element).

The aim of this study is to highlight the hydrogen trapping related to implantation-induced defects and thus characterize the interactions between hydrogen and these defects thanks to numerical simulations. For that, deuterium was used as a hydrogen isotopic tracer. The deuterium uptake was promoted in the 316L SS by room temperature cathodic charging.

Materials and Methods

Materials

Reference Material

An industrial grade of 316L SS was used in this study. Its chemical composition is given in Table 1. Large samples (110 mm x 22 mm x 1.5 mm) were cut by electrical discharge machining and then polished with SiC paper up to grade 1200. A first thermal treatment of 1 hour at 1080 °C, followed by oil quenching, was performed to annihilate dislocations and dissolve carbides. Then a second treatment of 15 hours at 300 °C was done to evacuate thermal vacancies possibly retained in the alloy during quenching. Thanks to these two thermal treatments, a reference material with a minimal quantity of defects was obtained. Coupons of 20 mm x 20 mm x 1.5 mm were then cut with a low-speed precision cut-off machine, to minimize the creation of new defects, and polished with SiC paper up to grade 2000 and diamond paste down to 3 µm followed by a mirror finish on a vibratory table with a suspension of colloidal silica.

	C	Si	Mn	S	P	Ni	Cr	Ti	Co	Al	Cu	Mo	Fe
Nominal	0.019	0.33	1.33	<0.003	0.025	10.36	16.94	0.024	0.10	<0.01	0.23	2.08	Bal.
Measurement uncertainty	± 0.003	± 0.01	± 0.02	-	± 0.003	± 0.15	± 0.15	± 0.003	± 0.01		± 0.01	± 0.03	-

Table 1: Nominal composition of the industrial 316L SS in wt.% obtained by Optical Emission Spectrometry

Implanted material

5 MeV Fe^{3+} ion implantations were performed on this reference material, at JANNuS-Saclay (Joint Accelerators for Nanoscience and Nuclear Simulation), CEA, France, to create sub-surface defects. An implantation temperature of 500 °C was used, in order to compensate for the effect of higher dose rate with ion irradiation on microstructural evolution, with a total dose of 4 x 10^{15} at.cm^{-2} and a mean flux of 7 x 10^{11} at.cm^{-2}.s^{-1}. Using SRIM Monte Carlo simulation code as detailed in Stoller's work [14], theoretical damages induced by implantation were estimated in dpa (displacement per atom). With our implantation conditions, damages reached up to 4.5 dpa at ~1.2 µm depth as presented in Figure 1.

Five Faraday cups were used in the specimen chamber to monitor the irradiation beam current. It was checked at every 10 min to extrapolate the actual value of implantation dose. Irradiation temperature was controlled by one thermocouple in the sample support and

monitored by an IR camera. The setpoint temperature had to be reduced at the beginning of the experiment to compensate for implantation-induced heating.
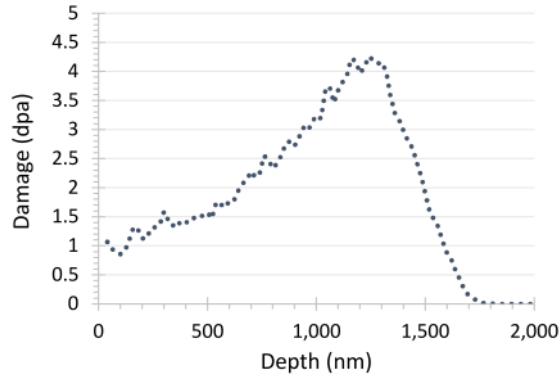

Figure 1 : SRIM calculation of the damage profile (dpa) for the Fe^{3+} implantation at 5 MeV and a dose of 4 x 10^{15} at.cm^{-2} used in this study

TEM observations

A Transmission Electron Microscopy (TEM) thin foil was prepared by the Focused Ion Beam (FIB) technique. This allowed us to characterize the distribution of implantation-induced defects in depth (from the surface).

TEM observations were carried out using a FEI TECNAI F20-ST field emission gun microscope operated at 200 kV. Irradiation-induced defects were characterized, particularly the Frank faulted loops. For that, the rel-rod dark field technique was used. The {111} stacking fault of each loop can produce rel-rods on the diffraction pattern. By tilting the TEM specimen, one rel-rod can be intensified (two beam condition) and used to image the corresponding Frank loops in dark field. This investigation technique is more detailed in [15].

Cathodic charging at 25 °C and aging

In order to study the interactions between implantation-induced defects and hydrogen, deuterium was introduced in the alloy by cathodic charging at 25 °C in a deaerated (Ar bubbling) 0.1 M NaOD solution. A cathodic current density j of 1 mA.cm^{-2} was chosen to enhance hydrogen adsorption on the surface from the proton discharge in Volmer-Tafel electrochemical domain.

Directly after cathodic charging, samples were quickly transferred and stored in liquid nitrogen (77 K) in order to prevent deuterium desorption and further internal diffusion. These specimens were then analyzed by Thermal Desorption Spectrometry (TDS) or by Secondary Ion Mass Spectrometry (SIMS). For this technique, an additional aging step of 24 h at 40 °C under vacuum was done to let a part of charged deuterium diffuse and desorb. All the charging and aging conditions are presented in Table 2.

	Solution	T [°C]	t [h]	j [mA.cm^{-2}]	Aging
TDS samples	0.1 M NaOD	25	1	1	/
SIMS samples	0.1 M NaOD	25	3	1	24 h at 40 °C

Table 2: Typical experimental deuterium cathodic charging and aging conditions

TDS

After deuterium cathodic charging, samples of reference material were analyzed by Thermal Desorption Spectrometry (TDS). It consists of monitoring the deuterium D_2 (m/z = 4) desorption flux as a function of time and temperature with a quadrupole mass spectrometer (Inficon™ Transpector 2). For this study, the specimens were subjected to a temperature ramp of 10 °C/min from room temperature to 1000 °C. Thanks to calibrated D_2 leaks, the signal given by the spectrometer (ionic current in $A.cm^{-2}$) can be converted into a quantified flux $(mol(D).cm^{-2}.s^{-1})$.

SIMS

SIMS (Secondary Ion Mass Spectrometry) analyses were conducted on deuterium charged and then aged samples with a CAMECA IMS7f device. A primary Cs^+ ion beam (40 nA) was used over a 125 x 125 µm² surface and the analyzed surface was limited to a 33 µm diameter circle via a system of diaphragms. Several elements were analyzed: ^1H, ^2H (or D), ^{12}C, ^{16}O, ^{52}Cr, ^{56}Fe, ^{58}Ni. To compare the results of the different samples by avoiding the influence of small variations of experimental parameters, the signal intensities were normalized to the highest signal (^{58}Ni) deep in the bulk.

After the analysis, the average crater depth was measured with a stylus profiler (Dektak$^©$, Bruker™), addressing an average sputtering rate used to convert the abrasion time (s) into depth from the surface (nm).

Results and Discussion

Microstructural characterization

Reference samples

After thermal treatments, the reference material was characterized by optical and electron microscopies. The mean grain size was estimated at 26 ± 6 µm from a polished and electrochemically attacked (oxalic acid) sample. The material presented an austenitic structure with around 3% of ferrite and scarce Ti(C, N) precipitates. A thin foil of the reference material was prepared by electrolytic thinning. TEM observations revealed the presence of some dislocation lines which were not counted, but their density being globally very low, the reference material will be considered defectless with respect to dislocations.

Fe^{3+} implanted samples

TEM observations were performed on a thin foil of a Fe^{3+} implanted sample. Figure 2 shows a TEM dark-field image of the sub-surface (surface is highlighted by the dashed line). It evidences the presence of faulted Frank loops with a wide range of sizes. Only one loop family on the existing four was characterized here which is assumed to represent 1/4 of the total number of Frank loops. The loop density and size were estimated as a function of their distance from the implanted surface as shown in Figure 3. Considering a thin foil thickness of about 100 nm, the total average density and mean diameter of dislocation loops observed on the whole implanted zone were estimated to be around $1 \pm 0.1 \times 10^{22} m^{-3}$ and 12.5 nm, respectively. The standard deviation related to the mean size of dislocation loops is 15 nm,

showing a high variability of the dislocation loops size. The mean size of Frank loops is similar to the values reported by Chen *et al.* (10-12.5 nm) and Miura *et al.* (9.5 nm), on 316 grade SS irradiated with 3 MeV Fe at 400 °C and 2.8 MeV Fe at 300 °C, respectively [16], [17]. The loop density was between a factor 10 and 100 lower in this study, which could be due to the higher irradiation temperature. For comparison, 10 MeV Fe implantation at 450 °C in Gupta *et al.* work [18] lead to an average loops density of 5 x 10^{21} m^{-3}, closer to the results of this study.
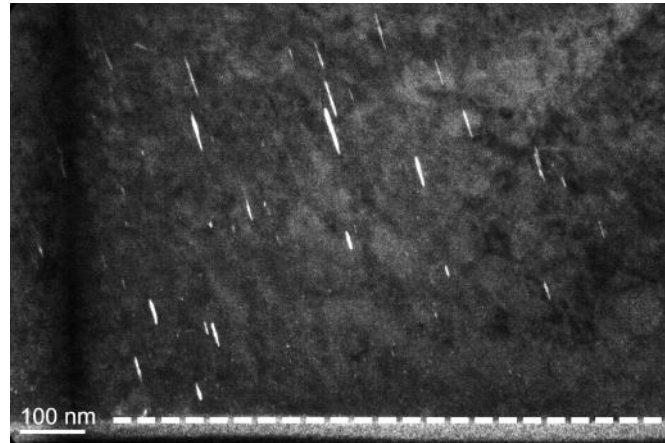

Figure 2: TEM dark field micrograph of the implanted zone near the surface (white dashed line at the bottom) evidencing Frank loops (white lines)
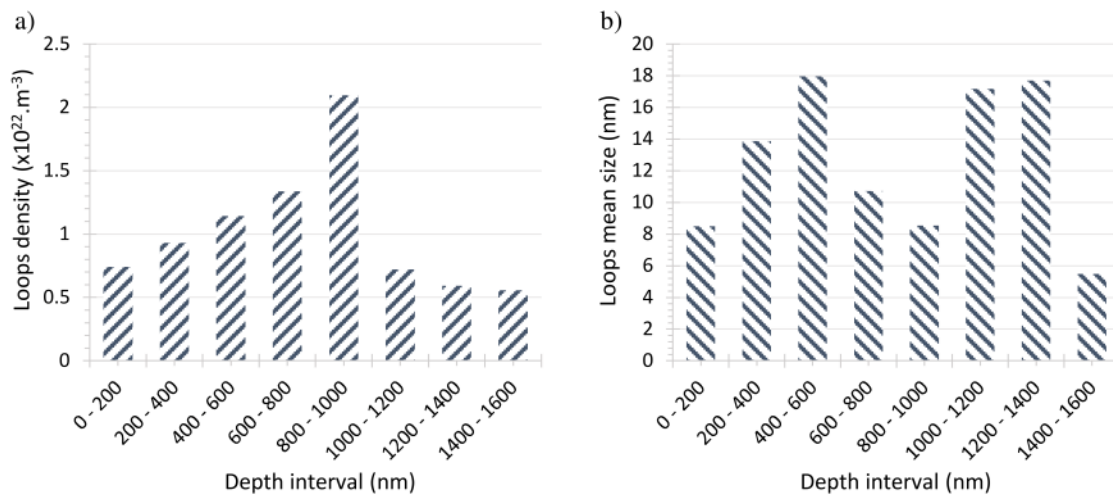

Figure 3: Evolution of Frank loops density (a) and mean size (b) as a function of the depth in the Fe^{3+} implanted sample

The shape of the loop density distribution is in good agreement with the damage distribution given by SRIM simulation for ion implantation even though the highest density of defects is shifted to lower depth between 800 and 1000 nm. An interesting thing to see is the decrease of the loop mean size between 600 and 1000 nm which could be related to the highest density of defects in this zone. There are more dislocation loops but they are smaller.

Besides, complimentary TEM observations, which would need further work, revealed the presence of numerous large cavities (up to diameter of 15 nm) in the implantation-affected zone as shown in the overfocused bright field image in Figure 4. Cavity population is not fully characterized yet but their density seems to be high between 650 and 1050 nm from the surface.
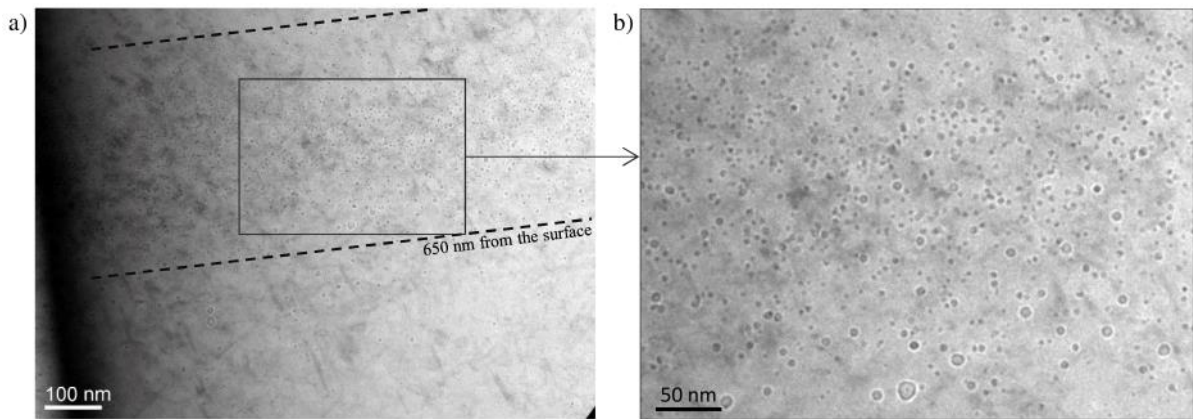
6

Figure 4: Bright field TEM micrographs in overfocused conditions of the implanted zone evidencing the presence of numerus cavities between 650 and 1050 nm from the surface (dashed lines), b) shows an area with cavities at higher magnification

Hydrogen trapping by irradiation-induced defects

The deuterium and hydrogen signals obtained by SIMS on the deuterium charged reference sample after 24 h aging at 40 °C are presented in Figure 5. Both signals are normalized to the ^{58}Ni signal and are not equivalent to concentrations because of the differences of sputtering and ionization rates. Hydrogen found in the specimen comes from the omnipresence of this element in the environment, mostly at the extreme surface, due to pollutions or water residues adsorbed on the surface. On the other hand, the deuterium profile, originating exclusively from the cathodic charging, shows an accumulation deeper in the alloy with a maximum for around 7 µm from the surface. This shape may be the result of deuterium interstitial diffusion during the aging step, out of the sample by its free surface and also deeper in the alloy (decreasing and shifting bell shape).
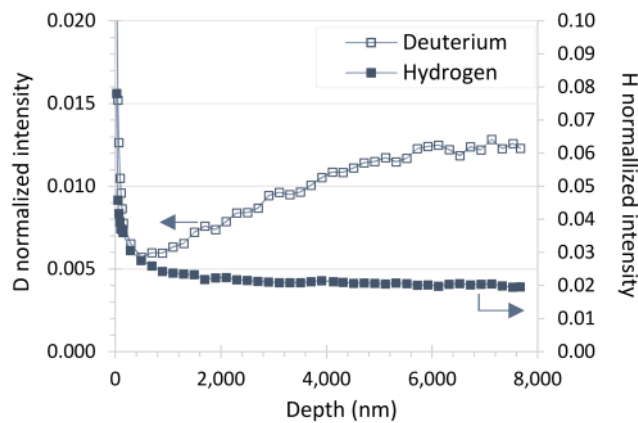

Figure 5: SIMS deuterium (empty squares) and hydrogen (full squares) profiles in a reference sample after D cathodic charging and aging for 24 h at 40 °C

SIMS analyses have also been conducted on the implanted sample after an identical deuterium charging and aging procedure. Figure 6 presents the deuterium profiles obtained on the charged implanted sample after aging, along with the one of the reference sample previously showed. It can be seen that, for the implanted specimen, a significant deuterium accumulation is observed between 600 and 1200 nm from the surface. This profile is in good agreement with the localization of implantation-induced defects and thus highlights the

trapping of deuterium by these defects. The non-trapped deuterium can still diffuse and lead, deeper in the alloy, to a residual profile similar to the one on the reference sample.

Hydrogen trapping by implantation-induced defects have already been evidenced by Jambon *et al.* [19] who worked on a nickel-base alloy and highlighted, thanks to SIMS analyses, hydrogen trapping related with defects induced by a previous Ni ion implantation.
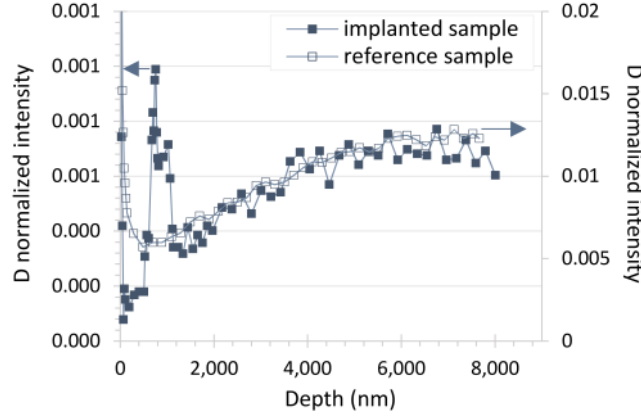

Figure 6: SIMS deuterium profiles of reference (empty squares) and implanted (full squares) samples after D cathodic charging and 24 h aging at 40 °C

Simulation of diffusion and trapping

To characterize the hydrogen trapping by irradiation-induced defects, a numerical model [20] was used to simulate the hydrogen diffusion and trapping in both implanted and non-implanted materials. For that, each experimental step, experimented by the samples, was taken into account in the simulations. To begin with, hydrogen diffusion coefficient in the studied SS was determined from the simulation of reference material experiments, then, thanks to additional trapping terms, hydrogen trapping by implantation-induced defects was simulated.

Determination of the diffusion constants

The first step to apply the numerical model on the implanted sample was to determine the pre-exponential constant D_0 and the activation energy E_a used to calculate, with an Arrhenius law, the diffusion coefficient (D) of the deuterium in 316L stainless steel (1). In this way, a "pure diffusion" system was considered and the classical Fick's second law (2) was used in the model to simulate the entire experimental sample history (i) cathodic charging by one surface under constant hydrogen surface concentration, then (ii) aging at 40 °C for 24 h in vacuum, under a null hydrogen surface concentration imposed by instantaneous surface recombination and release in vacuum of the desorbing hydrogen.

$$D = \mathbf{D_0} \, exp\left(\frac{-E_a}{RT}\right) \tag{1}$$

$$\frac{\delta C_L}{\delta t} = D \frac{\delta^2 C_L}{\delta x^2} \tag{2}$$

where C_L represents the local interstitial deuterium concentration.

Two experimental results on the defect-free reference material were used and simulated, then fitted thanks to D_0 and E_a adjustments. The first experiment used was a TDS deuterium spectrum (normalized to its maximum desorption rate) obtained with a reference sample just after a deuterium cathodic charging of 1 h at 25 °C (no aging) and the second one was the deuterium depth profile obtained by SIMS on a reference sample, deuterium-charged then aged at 40 °C for 24 h, as presented in the previous section.

All the experimental conditions of these experiments were incorporated into the modeling to be as close as possible to the reality in order to consider that there are only D_0 and E_a which can improve the simulated results. After adjustments of these constants from values given by the literature [21] to best fit the experimental TDS curve and then SIMS profile, a matching couple of values was found: $D_0 = 1.4$ x 10^{-5} cm².s^{-1} and $E_a = 40$ kJ.mol^{-1}. The comparison between experimental and simulated desorption curves considering this set of diffusion constants for the two experiments is shown in Figure 7. Some slight discrepancies between experimental and simulated results appear at the end of the deuterium desorption peak (figure 7a) and principally near the surface in the deuterium depth profile (figure 7b). These differences could originate from the fact that the reference material is not fully defect-free but this effect should be of the second order. The difference in the deuterium concentration profiles close to the surface may be assigned to the presence of a nanometric oxide layer on the surface, either inducing a barrier to H diffusion [22], [23] or limiting the recombination kinetics, two phenomena that were not taken into account in the modeling. However, there is globally a fairly good agreement between the experimental and the simulated data with the determined set of diffusion parameters.

These values determined here for the diffusion of deuterium in 316L stainless steel are in good agreement with literature data [24]–[27]. For instance, Forcey *et al.* found for the diffusion of hydrogen in an annealed 316L SS an activation energy of 42.5 kJ.mol^{-1} but a higher pre-exponential constant of 7.7 x 10^{-4} cm².s^{-1} (these values are assumed to be valid between 250 and 600 °C).
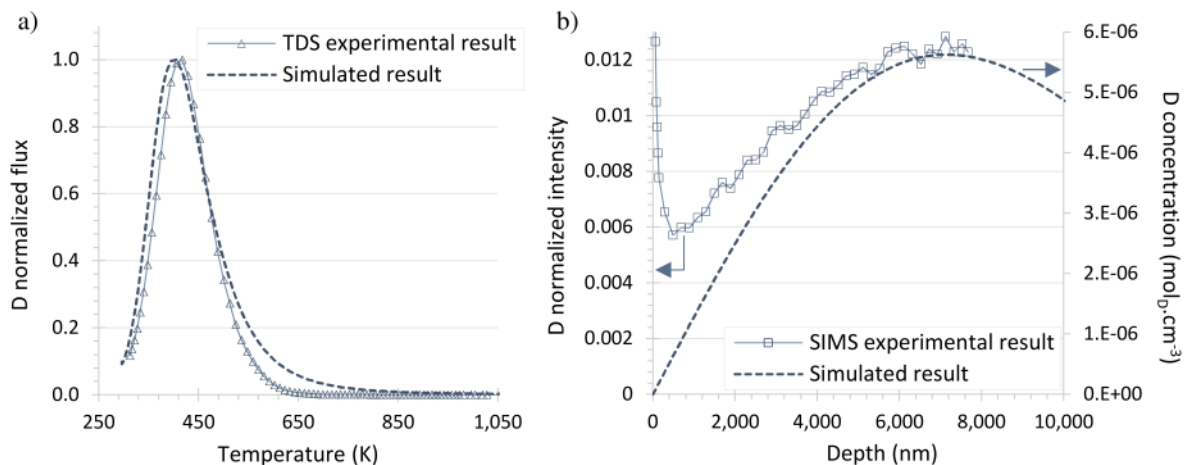

Figure 7: Comparison between experimental and simulated results for a) TDS deuterium spectrum just after cathodic charging and b) SIMS deuterium depth profile after cathodic charging and 24 h aging at 40 °C

Assuming interstitial diffusion is not affected by the presence of traps, provided they are considered a dilute system in the matrix, the diffusion parameters determined in this study with "pure diffusion" system were then directly injected in the numerical model for the simulation of diffusion and trapping of deuterium in the 316L stainless steel.

Diffusion and trapping of deuterium in the implanted material

To add the trapping phenomenon to the diffusion of deuterium in stainless steel, the set of McNabb and Foster's equations was used [28]. It corresponds to the second Fick's law with a trapping term (3) coupled with the kinetic equation of the deuterium trapping/detrapping (4).

$$\frac{\delta C_L}{\delta t} + N \frac{\delta \theta}{\delta t} = D \frac{\delta^2 C_L}{\delta x^2} \tag{3}$$

$$\frac{\delta \theta}{\delta t} = k(1-\theta)C_L - p\theta \tag{4}$$

where C_L represents the local interstitial deuterium concentration, N is the trap site density, θ the trap occupancy, D the interstitial diffusion coefficient, k and p the respective trapping and detrapping kinetic constants associated with one type of trap site, both following an Arrhenius law ((5) and (6)).

$$k = k_0 \, exp\left(\frac{-E_k}{RT}\right) \quad and \quad p = p_0 \, exp\left(\frac{-E_p}{RT}\right) \tag{5 and 6}$$

To start the simulation of deuterium diffusion and trapping by irradiation defects, only Frank dislocation loops were considered. The values of the parameters k_0, E_k, p_0 and E_p for dislocation loops did not exist in the literature but were available for edge dislocations in a nickel-based alloy in Hurley's work [21], see Table 3. Concerning the density of traps N, the experimental characterizations of the dislocation loops presented in section 3.1.2. were used. For practical reasons, we considered a dislocation loop of perimeter l equivalent to an edge dislocation of length l and so the dislocation linear density was calculated as a function of depth as shown in Figure 8. As explained in ref. [21], [29], [30], the experimental dislocation linear density can be converted into an amount of trap sites per volume unit in order to put it in the numerical model. The result of the simulation of deuterium depth profile after 3 h at 25 °C cathodic charging and aging for 24 h at 40 °C with these parameters is presented in Figure 9, along with the SIMS experimental deuterium profile. The experimental concentration profile is on average well-reproduced by the simulation using this preliminary set of parameters. Deeper than 3 µm from the surface, the two profiles are quite well-superimposed indicating a good reproduction by simulation of the interstitial deuterium profile, validating the hypothesis made on the invariance of diffusion coefficient. The zone where deuterium is trapped by implantation-induced defects is broader with simulation than in reality but the balance between interstitial and trapped deuterium is respected. With the current data, the trapping and detrapping kinetic parameters, k and p, extracted from literature, seem applicable to dislocation loops. However, since the only defects considered at the moment were dislocation loops, the simulation may be improved with considering also trapping of hydrogen by the cavities identified earlier in the paper. As cavities are significantly present in the depth range 600 – 1200 nm, which seems also to be the location of trapped deuterium on the SIMS concentration profile (Figure 9), their effect on trapping may need to be considered. On-going work is focusing on this subject.

Dislocations trapping (k)		Dislocations detrapping (p)	
k_0 (s^{-1})	E_k (kJ.mol^{-1})	p_0 (s^{-1})	E_p (kJ.mol^{-1})
$(1.5 \pm 0.2)\ 10^6$	42 ± 4	$(1.5 \pm 0.2)\ 10^6$	76 ± 4

Table 3: Trapping and detrapping kinetic constants for trapping at dislocations in A600 nickel-based alloy [21]
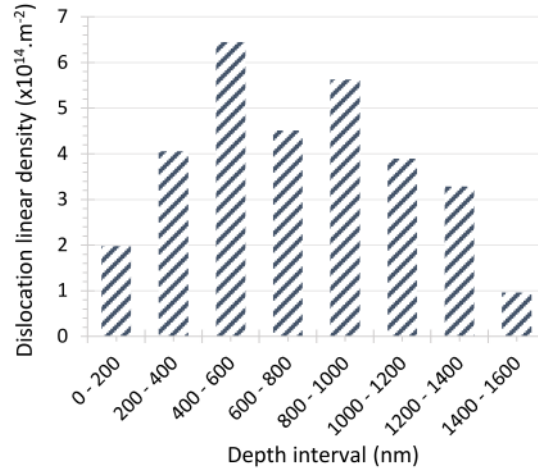

Figure 8: Evolution of the equivalent dislocation linear density as a function of depth in the implanted sample
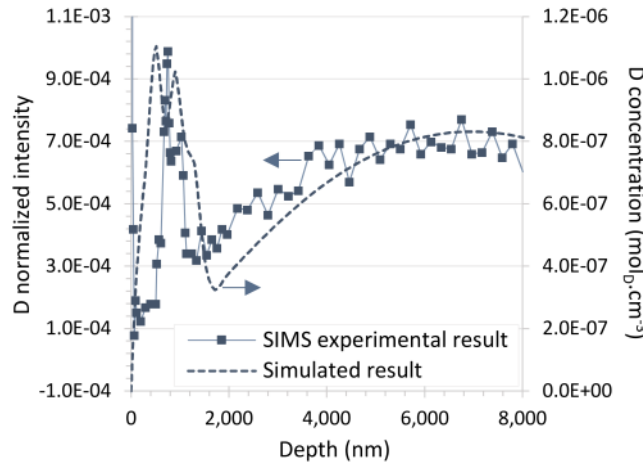

Figure 9: Comparison between SIMS (closed squares) and simulated (dotted line) deuterium depth profiles after cathodic charging of 3 h at 25 °C and aging for 24 h at 40 °C

Conclusion

In this work, to study the interactions between hydrogen and irradiation-induced defects, an annealed 316L stainless steel was implanted with 5 MeV Fe^{3+} ions at 500 °C in order to simulate defects created by neutron irradiation. The implanted microstructure was characterized by TEM and then deuterium cathodic charging and SIMS analyses allowed to focus on hydrogen trapping by implantation-induced defects.

SIMS analyses performed on both implanted and non-implanted model materials after deuterium cathodic charging and an aging step highlighted a strong trapping of hydrogen in link with the implantation defects but not in the whole implanted zone. A numerical model

used to simulate diffusion and trapping of hydrogen in materials was used to determine hydrogen interstitial diffusion coefficient and study trapping parameters. For that, the experimental conditions and real dislocation loop density were injected in the model. There is globally a fairly good agreement between the experimental and the simulated data using the following adjusted diffusion parameters: $D_0 = 1.4 \times 10^{-5}$ cm².s^{-1} and $E_a = 40$ kJ.mol^{-1}, and trapping parameters extracted from literature. Some differences remain certainly due to the presence of numerous cavities in the implanted zone which have not been taken into account in the model yet.

References

[1] P. Scott, Journal of Nuclear Materials, vol. 211, no. 2, pp. 101–122, 1994.

[2] G. S. Was, Y. Ashida, and P. L. Andresen, Corros. Rev., vol. 29, no. 1–2, pp. 7–49, Sep. 2011.

[3] M. Dumerval, S. Perrin, L. Marchetti, M. Tabarant, F. Jomard, and Y. Wouters, Corrosion Science, vol. 85, pp. 251–257, Aug. 2014.

[4] G. Pressouyre, Acta Metallurgica, vol. 28, no. 7, pp. 895–911, 1980.

[5] A.-M. Brass and J. Chene, Corrosion Science, vol. 48, no. 10, pp. 3222–3242, Oct. 2006.

[6] I. M. Robertson, P. Sofronis, A. Nagao, M. L. Martin, S. Wang, D. W. Gross and K. E. Nygren, Metallurgical and Materials Transactions B, vol. 46, no. 3, pp. 1085–1103, Jun. 2015.

[7] N. Hashimoto, E. Wakai, and J. P. Robertson, Journal of Electron Microscopy, vol. 48, no. 5, p. 575, 1999.

[8] D. J. Edwards, E. P. Simonen, F. A. Garner, L. R. Greenwood, B. M. Oliver, and S. M. Bruemmer, Journal of Nuclear Materials, vol. 317, no. 1, pp. 32–45, Apr. 2003.

[9] G. S. Was and P. L. Andresen, Corrosion, vol. 63, no. 1, pp. 19–45, 2007.

[10] O. K. Chopra and A. S. Rao, Journal of Nuclear Materials, vol. 409, no. 3, pp. 235–256, Feb. 2011.

[11] Y. Dong, B. H. Sencer, F. A. Garner, and E. A. Marquis, Journal of Nuclear Materials, vol. 467, no. 2, pp. 692–702, Dec. 2015.

[12] G. S. Was, J. T. Busby, T. Allen, E. A. Kenik, A. Jenssen, S. M. Bruemmer, J. Gan, A. D. Edwards, P. M. Scott and P. L. Andreson, Journal of nuclear materials, vol. 300, no. 2, pp. 198–216, 2002.

[13] G. S. Was, Fundamentals of Radiation Materials Science: Metals and Alloys. Springer Science & Business Media, 2007.

[14] R. E. Stoller, M. B. Toloczko, G. S. Was, A. G. Certain, S. Dwaraknath, and F. A. Garner, Nuclear Instruments and Methods in Physics Research, Section B: Beam Interactions with Materials and Atoms, vol. 310, pp. 75–80, Sep. 2013.

[15] D. J. Edwards, E. P. Simonen, and S. M. Bruemmer, Journal of Nuclear Materials, vol. 317, no. 1, pp. 13–31, 2003.

[16] D. Chen, K. Murakami, K. Dohi, K. Nishida, N. Soneda, Z. Li, L. Liu and N. Sekimura, Nuclear Instruments and Methods in Physics Research Section B: Beam Interactions with Materials and Atoms, vol. 365, pp. 503–508, Dec. 2015.

[17] T. Miura, K. Fujii, H. Nishioka, and K. Fukuya, Journal of Nuclear Materials, vol. 442, no. 1–3, Supplement 1, pp. S735–S739, 2013.

[18] J. Gupta, J. Hure, B. Tanguy, L. Laffont, M.-C. Lafont, and E. Andrieu, Journal of Nuclear Materials, vol. 476, pp. 82–92, 2016.

[19] F. Jambon, L. Marchetti, M. Sennour, F. Jomard, and J. Chêne, Journal of Nuclear Materials, vol. 466, pp. 120–133, Nov. 2015.

[20] C. Hurley, F. Martin, L. Marchetti, J. Chêne, C. Blanc, and E. Andrieu, International Journal of Hydrogen Energy, vol. 40, no. 8, pp. 3402–3414, 2015.

[21] C. Hurley, Ph-D thesis, Institut National Polytechnique de Toulouse, 2015.

[22] W. A. Swansiger and R. Bastasz, Journal of Nuclear Materials, vol. 85, pp. 335–339, 1979.

[23] R. Rios, T. Magnin, D. Noel, and O. de Bouvier, Metallurgical and Materials Transactions A, vol. 26, no. 4, pp. 925–939, 1995.

[24] P. Tison, Ph-D thesis, Université Pierre et Marie Curie Paris 6, 1984.

[25] C. Shan, A. Wu, and Q. Chen, Journal of Nuclear Materials, vol. 179, pp. 322–324, Mar. 1991.

[26] K. S. Forcey, D. K. Ross, J. C. B. Simpson, and D. S. Evans, Journal of Nuclear Materials, vol. 160, no. 2, pp. 117–124, Dec. 1988.

[27] D. M. Grant, D. L. Cummings, and D. A. Blackburn, Journal of Nuclear Materials, vol. 152, no. 2, pp. 139–145, May 1988.

[28] A. McNabb and P. K. Foster, Transactions of the metallurgical society of AIME, vol. 227, pp. 618–627, Jun. 1963.

[29] A. H. M. Krom and A. Bakker, Metallurgical and Materials Transactions B, vol. 31, no. 6, pp. 1475–1482, 2000.

[30] J. Chêne and A. M. Brass, Scripta Materialia, vol. 40, no. 5, pp. 537–542, 1999.